PAPER • OPEN ACCESS

2D FPCB micromirror for scanning LIDAR

View the article online for updates and enhancements.

You may also like

2D FPCB micromirror for scanning LIDAR

Trevor S Tai* , Siyuan He and Behrad Ghazinouri

Department of Mechanical and Industrial Engineering, Ryerson University, 350 Victoria Street, Toronto, Ontario, Canada

E-mail: tstai@ryerson.ca

CrossMark

Abstract

This paper presents a 2D flexible printed circuit board (FPCB) micromirror and a scanning 3D light detection and ranging (LIDAR) based on it by integrating the 2D FPCB micromirror with a commercially available single point LIDAR. The 2D FPCB micromirror retains the benefits of previously developed 1D FPCB micromirrors, i.e. large aperture and low cost while providing rotation of the mirror plate about two orthogonal axes to be able to scan a laser beam about both vertical and horizontal axes to achieve 2D scanning. One 2D FPCB micromirror is integrated with a single point LIDAR to achieve a 3D scanning LIDAR, which, in comparison to the previously developed 1D FPCB micromirror based 3D LIDAR, achieved more compact structure and easier fabrication/assembly due to no strict requirement on the alignment between two micromirrors while only one 2D micromirror rather than two 1D micromirrors used. Prototypes of the 2D FPCB micromirror and the 3D LIDAR based on it are fabricated and tested. The test results demonstrate that the 2D FPCB micromirror based 3D LIDAR achieved a volume reduction over the previous 1D FPCB micromirror based 3D LIDAR from 1042 cm^3 to 754 cm^3 with a field of view of $40° \times 24°$ at 150 Hz horizontal scanning and 2 Hz vertical scanning.

Keywords: 2D FPCB micromirror, 3D LIDAR, Micromirror scanning LIDAR, Large aperture micromirror

(Some figures may appear in colour only in the online journal)

1. Introduction

Light detection and ranging (LIDAR) is an advancing technology of interest in the field of autonomous vehicles on roads and automated guided vehicles (AGVs) for applications in the manufacturing and logistics industries [1–4]. 3D maps of a surrounding environment can be obtained using a scanning LIDAR. Traditional scanning LIDARs depend on motor-based scanning mechanisms which come with disadvantages of a bulky and heavy structure, low reliability, high power consumption as well as high cost due to an array of emitting lasers/receivers required to achieve multiple-line scanning as well as the expensive motors/encoder required long time and continuous accurate rotating [1, 5]. Microelectromechanical systems (MEMS) mirrors are currently drawing interest as an alternative component in motor-based scanning LIDARs with advantages of significantly lower cost, lighter weight, more compact size, higher reliability (no macro rotation part) and lower power consumption [2, 6, 7], after various MEMS micromirrors have been successfully developed and applied to display, bio-medical imaging, communication, and LIDAR [8–19].

A new type of MEMS micromirror technology, i.e. flexible printed circuit board (FPCB) micromirror, was developed in our group since 2016 [20–31], which uses (a) the flexible

---

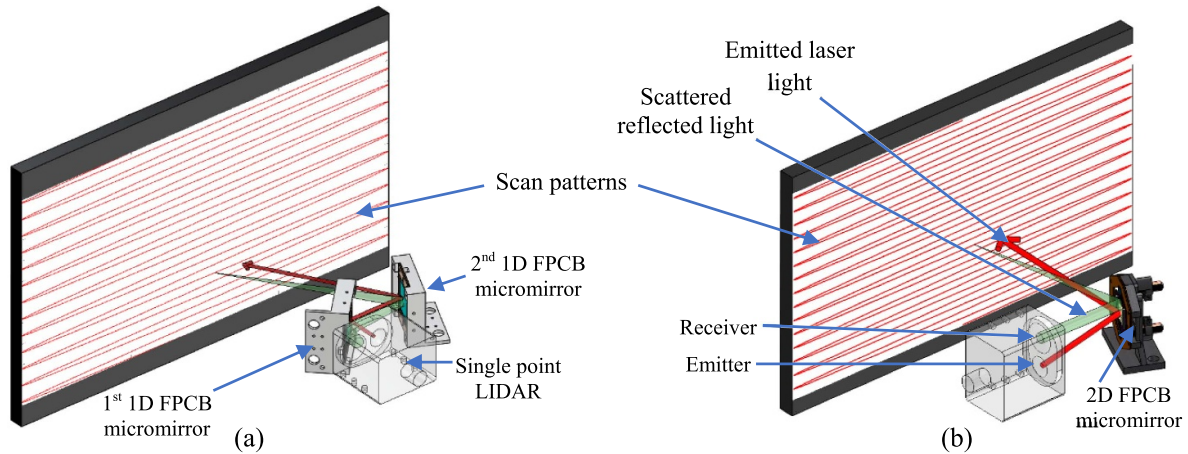* Author to whom any correspondence should be addressed.

Figure 1. FPCB micromirror based scanning 3D LIDAR. (a) Two 1D FPCB micromirrors based scanning 3D LIDAR. (b) One 2D FPCB micromirror based scanning 3D LIDAR.

printed circuit board as the supporting substrate and flexible structure (e.g. torsion beams), (b) the embedded copper coils as the driving element to generate oscillating Lorentz forces, and (c) a metal film coated silicon plate diced off a silicon wafer as the mirror plate to be bonded to the FPCB supporting substrate. Since the mirror plate is separately fabricated and then bonded to the FPCB structure, a large aperture can be achieved, e.g. 1 mm to >10 mm. The FPCB micromirror technology has the advantage of very low cost due to the usage of mature FPCB industrial process instead of the expensive micromachining processes except for the low-cost fabrication of the silicon mirror plate which requires only thin metal film coating and silicon wafer dicing. Various 1D FPCB micromirrors have been developed for different applications as reported in [25–29]. 1D FPCB micromirrors can generate rotation of the mirror plate about one axis to scan the laser beam such as to turn a single point LIDAR into a line scanning 2D LIDAR [21, 25, 26, 28, 29, 31]. Two 1D FPCB micromirrors can be cascaded to realize 2D scanning, i.e. the 1st 1D FPCB micromirror for vertical scanning and the 2nd 1D micromirror for horizontal scanning as shown in figure 1(a). The two 1D FPCB micromirrors constructed 2D scanner can be integrated with a single point LIDAR to form a scanning 3D LIDAR as reported in [25, 29–31]. However, the 2D scanner based on two 1D FPCB micromirrors is bulky. In addition, the two 1D micromirrors in the 2D scanner must be well aligned. Otherwise, the laser beam scanned by the 1st 1D FPCB micromirror would be off the 2nd 1D FPCB micromirror. Consequently, the maximum vertical scanning angle is limited by the aperture size of the 2nd 1D FPCB micromirror and the alignment between the two 1D FPCB micromirrors. Thus, a 2D FPCB micromirror, in which the mirror plate rotates about two axes to realize both vertical and horizontal scanning is highly desired, which does not require strict alignment between two micromirrors with the vertical scanning angle not limited by the 2nd micromirror's aperture and the alignment between two micromirrors. In addition, the total size and cost of the 2D scanner can be decreased when using a 2D micromirror

over two 1D micromirrors. This paper proposes a 2D FPCB micromirror design, which retains the benefits of previous 1D FPCB micromirrors, i.e. large aperture and low cost while providing rotation of the mirror plate about two orthogonal axes to be able to scan a laser beam about both vertical and horizontal axes to achieve 2D scanning with one micromirror. Thus, the 2D FPCB micromirror can be integrated with a single point LIDAR to achieve a 3D scanning LIDAR (as shown in figure 1(b)) with a more compact structure and lower cost with no strict requirement on the alignment between two micromirrors over the previous two 1D FPCB micromirrors based 3D scanning LIDAR [30].

In the paper, section 2 introduces the design and principle. Section 3 presents the modeling and simulation. Section 4 describes the application of the 2D FPCB micromirror to 3D scanning LIDAR. Section 5 presents the prototype and testing of the 2D FPCB micromirror and the 3D LIDAR based on it. Conclusions are in section 6.

2. Design and principle

2.1. Design of the 2D FPCB micromirror

As shown in figure 2, the 2D FPCB micromirror has the mirror plate seated on an FPCB substrate with embedded copper coils, two plate permanent magnets are located beside the coils to generate the Lorentz force on the coils when the current is applied to the coils. As a result, the Lorentz force oscillates the mirror plate about the inner axis. The mirror plate is supported by the rectangular gimbal, which is rotated about the outer axis by the electromagnetic forces generated between the two permanent magnet discs and the two underneath solenoids. The two permanent magnet discs are bonded to the two tips of the gimbal with two solenoids underneath the permanent magnet discs. Thus, the mirror plate's oscillation (frequency and amplitude) about the inner axis is controlled by the current though the coils embedded in the FPCB substrate and the oscillation about the outer axis is controlled
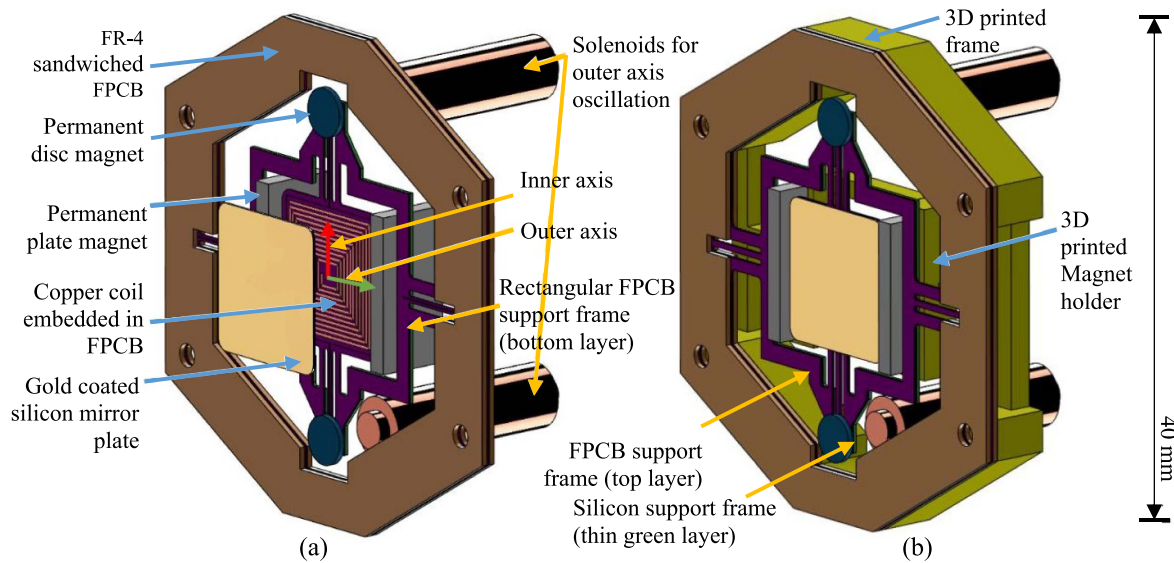
Figure 2. Design of the 2D FPCB micromirror. (a) 2D FPCB micromirror without assembly structure (b) 2D FPCB micromirror with assembly structure.

by the current applied to the solenoids. The oscillation about the inner axis is at the frequency close to the natural resonant frequency to realize a large oscillation angle (e.g. ∼150 Hz and max optical angle of ∼60°), which is always used for horizontal laser scanning, while the oscillation about the outer axis is at the frequency far below its natural resonant frequencies and thus is quasi-static rotation (e.g. 2.5–5 Hz), which is usually used for vertical laser scanning. According to the above working principle, the mirror plate can rotate about two orthogonal axes, i.e. the inner and outer axes, to realize 2D laser scanning if a laser beam is shot on to the mirror plate. In addition, the 2D FPCB retains the benefits of the previous 1D FPCB micromirror, i.e. large aperture (e.g. >10 mm in square).

2.2. 3D scanning LIDAR

As shown in figure 1(b) the 2D FPCB micromirror is integrated with a single point LIDAR to form a 3D scanning LIDAR. The 2D FPCB micromirror has a large aperture (12 mm × 12 mm) to both scan the emitting laser from the single point LIDAR horizontally and vertically in the 3D space and receive the scattered-reflected light from the object and reflected the light to the single point LIDAR's receiver. The mirror's rotation can be defined as the following: inner axis rotation is the oscillation about the vertical axis torsion beams which drive the mirror to scan horizontally, and outer axis rotation is the oscillation about the horizontal axis torsion beams which drive the mirror to scan vertically.

The mirror has an aperture of 12 mm × 12 mm and when aligned with the single point LIDAR it can scan in two rotational axes as shown in figure 2. The single point LIDAR is aligned at a 30° angle to the mirror to increase the amount of scanned light and received diffuse reflected light. The inner

axis scan can reach 40° optical angle oscillating in a sine pattern at a resonance of 150 Hz, while the outer axis scan can reach 24° at a quasi-static 5 Hz in a triangular pattern. With the mirror simultaneously rotating in both axes, a 3D LIDAR map can be obtained.

The optical path can be seen in figure 1(b). As the infrared laser beam from the single point LIDAR exits the emitter in a straight line, the mirror reflects the beam in a 2D sinusoidal pattern and scattered reflected light from this pattern is captured by the FPCB 2D micromirror and reflected to the single point LIDAR's receiver and sampled at 10 000 points per second as single points along the sinusoidal pattern. Thus, a minimum of 1000 points are required at 5 Hz to build a single 'image' of a scene that's covered by the 2D scan pattern. However, a 2000-point sample is better as it includes the forward and backward sweep of the mirror which helps in aligning the image accurately.

A position sensitive detector (PSD) is mounted to the back of the 2D FPCB micromirror, which in combination with a small silicon circular mirror attached to the backside of the FPCB structure, can detect the rotation angle along both horizontal and vertical directions. The general method of using a 1D PSD to measure 1D FPCB micromirror's rotation angle is introduced in [30]. The method used to obtain the mirror plate's rotation angles about along two directions in a real time mode uses a single 1D PSD to derive both horizontal and vertical oscillation angles is presented in [32]. The details of the PSD measurement setup are shown later in section 5.

3. Modeling and simulation

The simulation of the 2D micromirror requires a model to be used in static analyses. Figure 3 shows a modification applied the model to simplify and accelerate the simulation process.
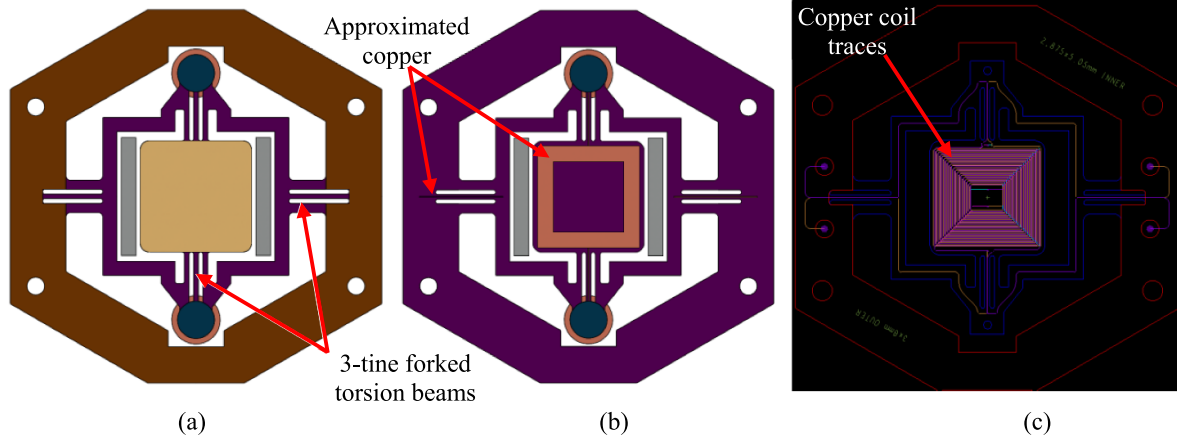
Figure 3. FPCB simulation and layout models. (a) Top view. (b) Section view. (c) PCB layout.

The copper coil traces shown in the PCB layout of figure 3(c) is simplified to a copper plate in the center of the mirror platform in figure 3(b). In addition to this, the simulation leaves out the FR-4 frame as it is assumed to be a static body.

The FPCB substrate follows a similar manufacturing process as the 1D FPCB micromirror [30], which consists of five polyimide layers totaling 169.5 μm in thickness with four layers of embedded copper ($\sim$18 μm thick each layer). The mirror plate is made of 200 μm thick silicon with 100 nm gold film coated. There are 21 turns of copper coil with line width of 0.1 mm. For simplicity in the simulation, a 36 μm thick copper layer is sandwiched between two 84.75 μm thick polyimide layers. The polyimide layers in the simple simulation together make up the same thickness as the real version, and the copper layers were simplified as a plate that's half the total thickness of 72 μm but is the same total mass. The reason the simulated copper thickness does not match the design is due to keeping the copper thinner for the simulation and to keep the mass distribution close to the design as the plate model is denser than the coil model.

Similar to [30], the design of the torsion beams is 3-tine forked as shown in figure 3(a). The reason the torsion beams of three-pronged slices are termed '3-tine forked' is to describe the difference of this design compared to a singular beam. The definition of 'forked' here is having a divided path between two points. The two additional slices to the sides of the middle slice allows for a greater distribution in stress along all three beams to reduce the stress in the embedded copper. This also has the effect of increasing the resonant frequency. The material properties used in the simulation are shown in table 1. For the magnetostatic simulation section, the BH curve used is for a N52 neodymium magnet [33]. The inner 3-tine forked flexure's middle beam has the dimension of 5.5 mm in length, the outer two beams are 3.38 mm in length. All three beams of the inner 3-tine forked flexure have a width of 0.5 mm. The outer torsion 3-tine forked flexure has the middle beam length of 6.5 mm with 0.5 mm in width, outer beams length of 4 mm with 1 mm in width. The inner

Table 1. Material properties used in simulation.

Material	Density (kg m^{-3})	Young's modulus (GPa)	Poisson's ratio
Copper	8300	110	0.34
Polyimide	1420	2.5–4 [34, 35]	—
Silicon	2330	169	0.28
Gold	19 320	77.2	0.32

torsion beam's stiffness is: 1.74×10^{-3} N·m rad^{-1} (for polyimide Young's modulus of 4 GPa) 1.13×10^{-3} N·m rad^{-1} for polyimide Young's modulus of 2.5 GPa. Outer torsion beam: 5.39×10^{-3} N·m rad^{-1} (for polyimide Young's modulus of 4 GPa) 3.4×10^{-3} N·m rad^{-1} for polyimide Young's modulus of 2.5 GPa.

3.1. Modal simulation

The modal simulation is conducted in ANSYS 2020R1 [36]. The resulting modes are shown in figure 4 and the frequency of each mode is listed in table 2. Note that the Young's modulus of polyimide was simulated at 2.5 GPa and 4 GPa due to the nature of the material being variable [34, 35]. Thus, simulations were done for both settings to acquire the potential range of results to be expected in manufacturing. Modes 1 and 2 are the modes of resonance that are relevant to the present 2D FPCB micromirror design. Mode 2 shows the resonance about the inner axis, i.e. for the horizontal scanning. Mode 1 sets the boundary for outer axis (i.e. vertical scanning) oscillation as it operates quasi-statically and at most operates at 15 Hz, which should be much lower than its resonant mode for the number of scanning lines to be reasonably high. This is because the number of scanning lines is proportional to the ratio between the fast and slow scanning axes and is further discussed in section 3.4. Modes 3 and 4 also set the boundary on stable operating modes, as the operating frequency of either axis must avoid being exited in unstable modes. While
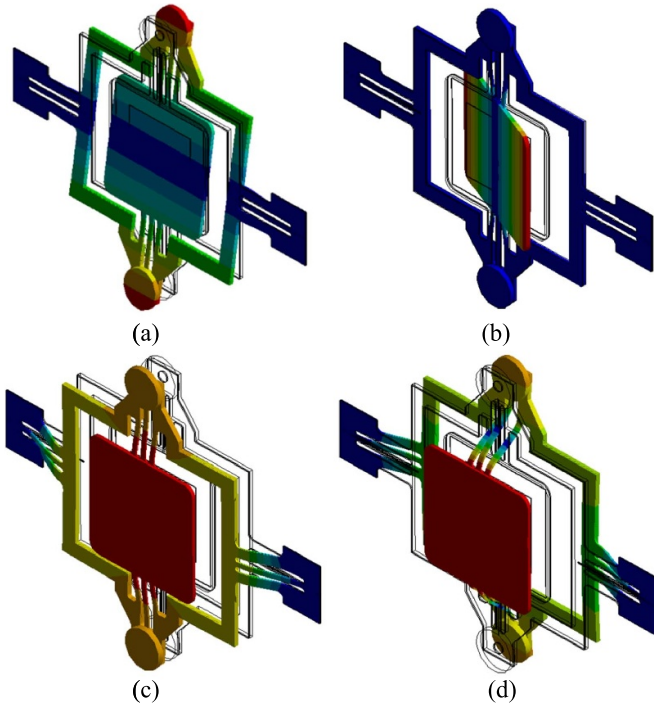
Figure 4. Resonant vibration modes. (a) 1st mode. (b) 2nd mode. (c) 3rd mode. (d) 4th mode.

Table 2. Resonant frequencies of different modes.

Mode	2.5 GPa polyimide frequency (Hz)	4 GPa polyimide frequency (Hz)
1st	45	56
2nd	143	180
3rd	159	194
4th	436	541

mode 3 is close to mode 2, during experimentation as shown in section 5.2, mode 3 is not excited. Mode 4 is out of range from the operating frequencies of the 2D micromirror.

3.2. Static simulation of the oscillation about the inner axis

The static simulation is conducted in ANSYS 2020R1. This simulation is used to characterize the mirror's rotation angle. The Lorentz forces acting on the mirror are calculated as follows. The simulation environment places the 12 mm × 12 mm mirror between the two N52 neodymium magnets [33] and calculates the magnetic flux density on the mirror. Since the Lorentz forces only act on the coils perpendicular to the field, the magnetic flux density is measured at the location of the coils over the mirror plate starting from 1.3 mm from the center to 11.2 mm in 0.2 mm increments for 21 turns. The coil plane's length along the magnetic field direction is 10.6 mm, the coil plane is 1.14 mm away from the magnet and in the middle between the two magnets. In figure 5, the magnetic field is along the *x*-axis and thus, only forces for the coil segments along the *z*-axis are summed as they are orthogonal to the field. The path of interest is shown in figure 5(b), starting from 1 (center of plate) to 2 (edge of plate). With the additional

knowledge that the resistance of the entire copper coil is 32 Ω, these values are then used to calculate the Lorentz force at that section of wire by equation (1) [37]

$$F_L = ILB\sin(\theta) \tag{1}$$

where *I* is the current (A), *L* is the length of coil segment perpendicular to the field (m), and *B* is the magnetic flux density (T) and θ is the angle of the normal to the coil plane with respect to *B*.

After calculating the Lorentz force, the torque can then be calculated by multiplying the distance from the center of the mirror platform to the specific coil location. This is done for the 21 segments of copper coil.

In order to create a trend for this simulation, several test voltages are chosen as inputs (1 V, 2 V, 4 V, 6 V & 8 V) and for each voltage, the Lorentz force and torque at each of the 21 segments are calculated. A summation of the torques for each voltage test is then applied to a static force simulation model to calculate the displacement. With this displacement, the angle can be calculated with trigonometry. Some adjustments are required before the final angle is calculated such as scaling the result to four copper layers and accounting for both sides of the micromirror. Figures 6–8 show the process of gathering the simulated data for magnetic flux density and torque for each coil segment to calculating the torque vs. angle for polyimide. These torques correspond to an angle of 0°. Figure 9 is the result of applying torques to the mirror model to calculate the angle and a comparison to the experimental results.

3.3. Oscillation about the outer axis

The outer axis oscillation uses solenoids pushing and pulling forces simultaneously on N52 neodymium disc magnets to oscillate the 2D FPCB micromirror along the outer axis. In order to simulate the static rotation angle, the force acting on the disc is approximated with equation (2)

$$F_{slnd} = \frac{(n \times I)^2 \times u_0 \times A}{2g^2} \tag{2}$$

where *n* is the number of turns in the solenoid, *I* is the current applied to the solenoid (A), u_0 is the relative permeability of air, *A* is the cross-sectional area of the solenoid (m^2), and *g* is the distance of the gap between the solenoid and the magnet (m). Note that equation (2) is an approximation and will break down for larger gap distances and for finite angles of the magnet. The solenoid has a resistance of 29 Ω, radius of 2 mm, 534 turns, and the gap between the solenoid and the disc magnet is 4.3 mm as shown in figure 10(a). The distance from the center of a disc magnet to the center of the mirror platform is 13.275 mm. The inductance caused current change is not considered due to the low oscillation frequency (<200 Hz) and small inductance (e.g. <500 μH).

Similarly to the inner axis, by using several test voltages (1 V, 2 V, 4 V, 6 V and 8 V), the force of the solenoid for each voltage can be calculated using equation (2) to create a trend. With the force of the solenoid calculated, the torque can also
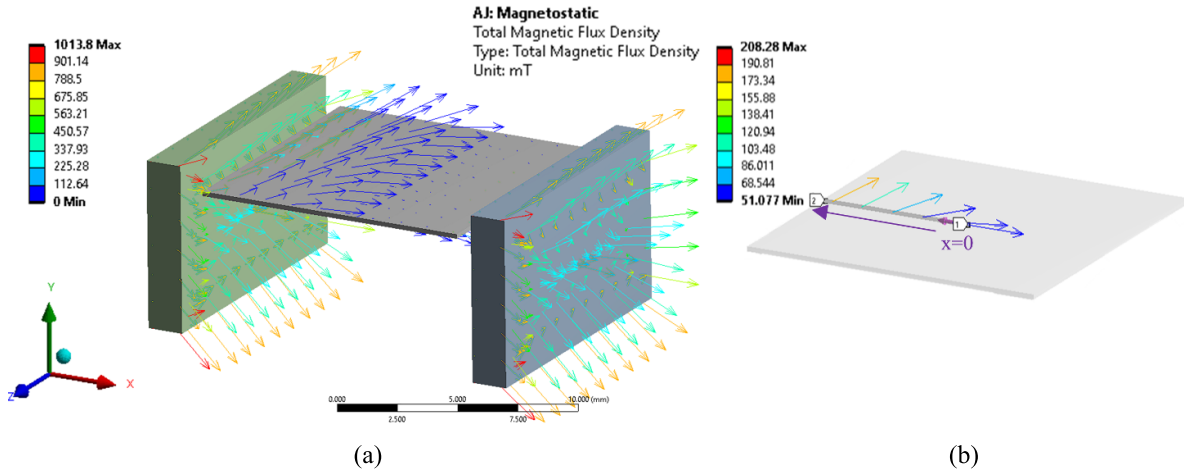
Figure 5. Inner axis static simulation: magnetic flux density simulation. (a) The whole structure (b) the place between magnets with coils.
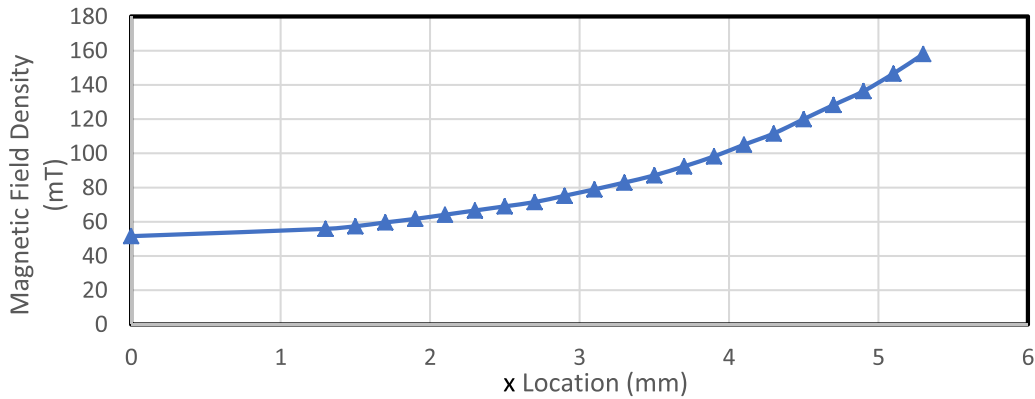

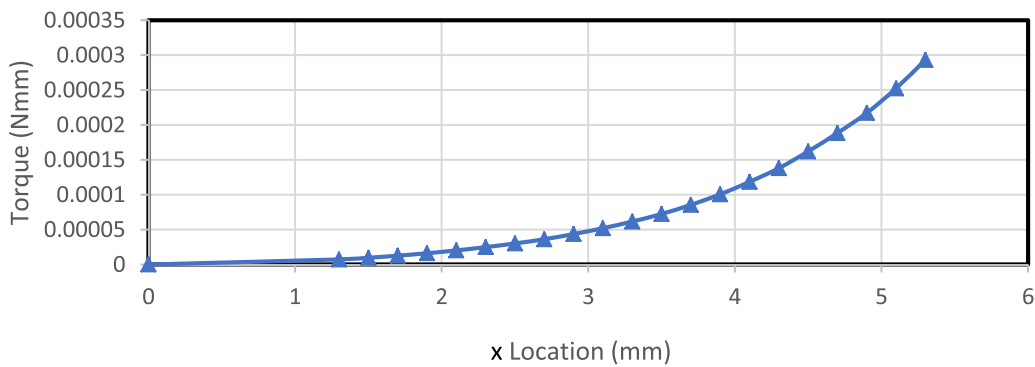**Figure 6.** Magnetic field density vs. *x* distance ($z = 0$).

Figure 7. Torque vs. *x* distance ($z = 0$).

be calculated by multiplying the force by the distance between the center of the mirror platform to the center of a disc magnet, of which is co-linear with the solenoid. This torque is then doubled for both sides and used in a static simulation model to calculate displacement and thus, the angle can be calculated. The relationship between voltage and angle is shown in figure 10(b). The gaps on both sides for a maximum angle of 10° are 1.96 mm and 6.64 mm respectively.

3.4. 3D LIDAR based on the 2D FPCB micromirror's point cloud performance calculation

This part calculates the 3D scanning LIDAR performance such as the number of scanning horizontal lines, refreshing frame rate, number of points in each frame and the theoretical maximum outer and inner axes scanning angle according to the geometric limitations. The mirror oscillates about the inner
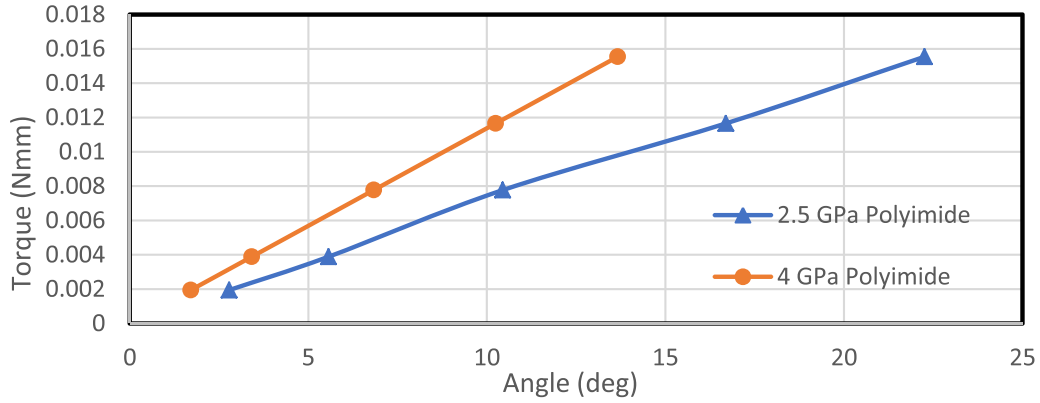
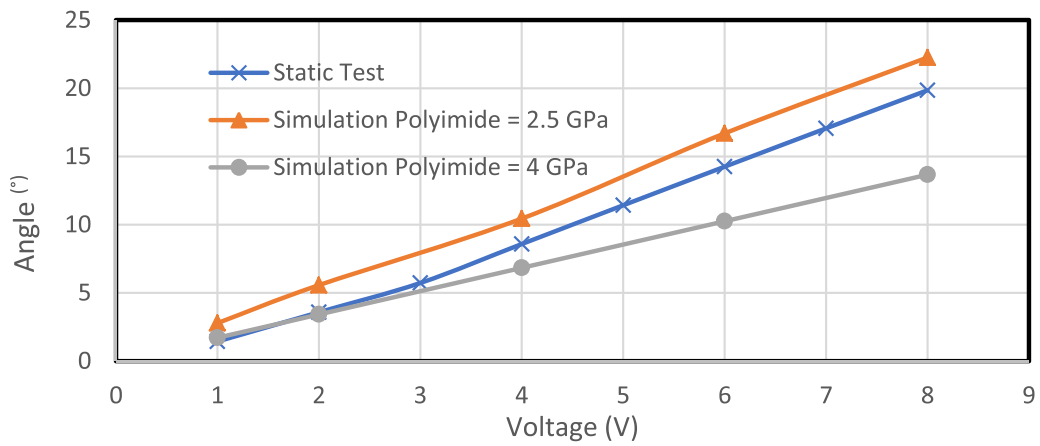**Figure 8.** Torque vs. angle (plate at $0°$).

Figure 9. Inner axis static rotation angle vs voltage.

axis at 150 Hz in a sinusoidal trajectory and about the outer axis at 2.5–5 Hz in a triangular trajectory. With both axes rotating simultaneously, the following 2D scan pattern in figure 11 is projected by a visible beam. An infrared beam will follow this pattern under normal operation.

The oscillation about the outer axis is quasi-static and is the limiting factor in determining the scanning rate of the LIDAR system. As the mirror rotates about the outer axis at 2.5–5 Hz, the inner axis is scanning at a much faster frequency (150 Hz) and can capture details during scans. The horizontal scanning lines and refreshing frame rate are determined by the display plot modes, i.e. Half_period mode or Full_period mode. The calculation method is the same as [30] with the same single point LIDAR and as such, the steps are repeated here for convenience.

Plotting of half_period mode means every frame includes single point LIDAR measurement data acquired during half the triangular trajectory, e.g. either upward or downward sweep. The plot of full_period mode means every frame includes single point LIDAR measurement data acquired during the oscillation of full triangular trajectory, e.g. both upward and downward sweep.

In half_period plot mode the horizontal scanning line number and refreshing rate are expressed in equations (3) and (4)

$$n_{\text{half\_period}} = \frac{f_v}{2 \cdot f_h} \qquad (3)$$

$$r_{\text{half\_period}} = 2 \cdot f_h \qquad (4)$$

where $n_{\text{half\_period}}$ is the number of horizontal scan lines, $r_{\text{half\_period}}$ is the refresh rate, f_v is oscillation frequency about the inner axis and f_h is the oscillation frequency about the outer axis. In the plot of full_period mode, the following equations (5) and (6) hold

$$n_{\text{full\_period}} = \frac{f_v}{2 \cdot f_h} \qquad (5)$$

$$r_{\text{full\_period}} = f_h \qquad (6)$$

where $n_{\text{full\_period}}$ is the number of horizontal scan lines, $r_{\text{full\_period}}$ is the refresh rate. Half_period mode leads to double the refreshing rate compared to full_period mode. However, the full_period mode normally renders double the data points per frame because during Mirror 1's upward or downward scanning sweep, the measurement points are taken by the single-point LIDAR instead of waiting for both
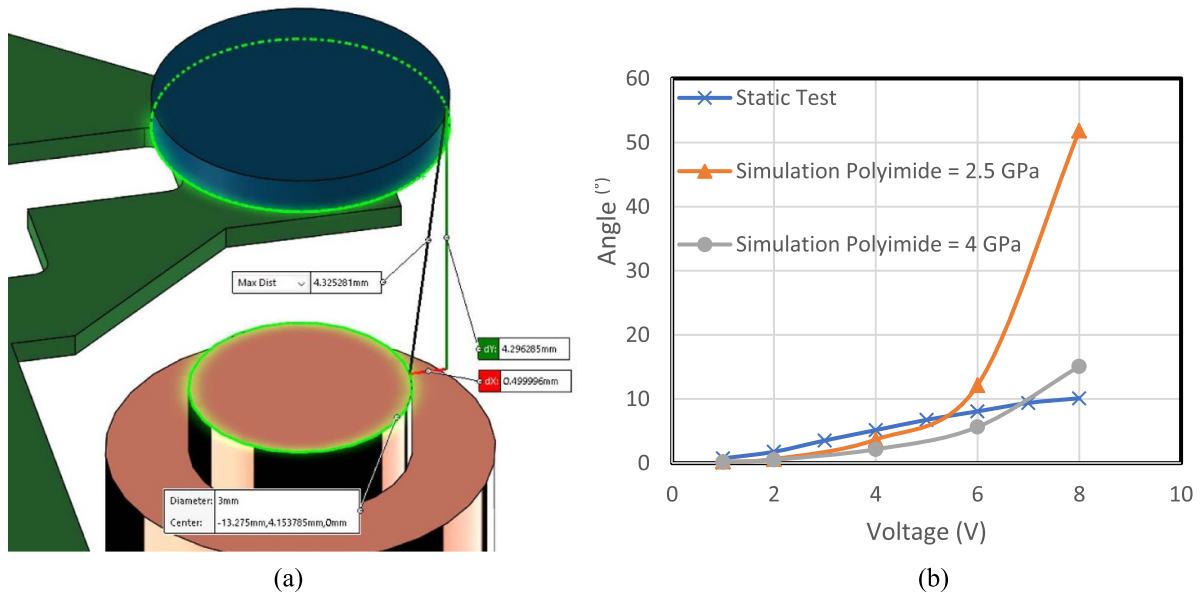
Figure 10. Outer axis oscillation static simulation. (a) Model showing disc and solenoid spacing. (b) Outer axis static rotation angle vs. voltage.

Figure 11. Raster scan pattern (visible laser) with 150 Hz sinusoidal and 5 Hz triangular waves.

upwards and downwards scanning sweep in full_period mode. The single point LIDAR (TF03) generates 10 000 measurement points per second. Thus, the number of horizontal scanning lines, frame refreshing rate and number of data points per frame can be calculated with the results listed in table 3.

4. Circuit and data processing in the 3D LIDAR based on the 2D FPCB micromirror

In the 2D FPCB micromirror based 3D LIDAR, a live 3D point-cloud map is derived using a single PSD. This method uses a 1D PSD to track the oscillation angles about both the

Table 3. Number of horizontal scanning lines, frame rate and number of data points per frame.

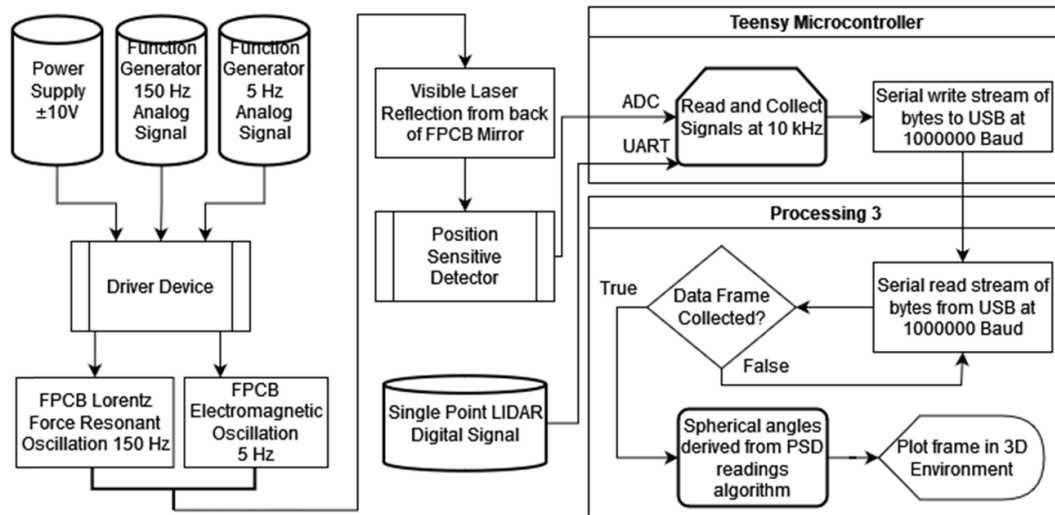| Outer axis frequency (Hz)	Inner axis frequency (Hz)	Plot mode	Refresh rate (fps)	Number of horizontal lines	Data points per frame	Points per line	Horizontal angular resolution	Vertical angular resolution
2.5	150	Full_period	2.5	30	4000	133.3	0.3°	0.09°
2.5	150	Half_period	5	30	2000	66.6	0.6°	0.18°
5	150	Full_period	5	15	2000	133.3	0.3°	0.09°
5	150	Half_period	10	15	1000	66.6	0.6°	0.18°

Figure 12. Data flow diagram in the 3D LIDAR based on the 2D FPCB micromirror.

inner and outer axes using the method reported in [32]. The PSD used in this prototype is the 1L10 from On-Trak [38]. The data flow diagram of the 3D scanning LIDAR based on the 2D FPCB micromirror is shown in figure 12.

The mirror oscillates about the outer and inner axes at 2.5–5 Hz and 150 Hz simultaneously. The frequency generator that outputs the signals for both axes are synchronized. With the use of a small mirror attached to the FPCB backside and a visible laser, the visible laser is behind the 'perf board' to pinhole the beam and is reflected off the small silicon mirror onto the 1D PSD (mounted to perf board) as shown in figure 13(e). The 1D PSD is meant for tracking in 1D, but with the use of an algorithm developed in [32], both angles necessary for spherical coordinates can be calculated along with the distance from the single point LIDAR. With this method, three key pieces of data are collected at the microcontroller: PSD signal (Analog), LIDAR distance (Digital) reading and timing. This data is then sent through USB to a computer for further processing. On the computer, the received data is collected, the spherical angles are calculated and are then converted to Cartesian coordinates to be plotted in real-time in 3D space. Note that in figure 12, analog to digital converter and universal asynchronous receiver-transmitter are protocols used to send data to the microcontroller.

5. Prototype and test

5.1. Manufacturing the 2D FPCB micromirror

The 2D FPCB micromirror structure and the assembled device are shown in figure 13. The supporting assembly black frame structure was manufactured using a 3D printer to support the micromirror.

Details of assembling the 2D FPCB micromirror prototype are as follows.

(a) Slot the rectangular magnets into their holding slots in the 3D printed structure with glue
(b) Use adhesive (glue/double-sided tape) to bond the metal coated silicon mirror plate to the center of the FPCB substrate/platform
(c) Use adhesive to bond a small silicon mirror to the backside of the FPCB substrate/platform
(d) Glue the disc magnets to the ends of the gimbal tips where they will align co-linearly with the holes
(e) Place the FPCB platform onto the 3D printed structure and screw in the holes along the FR-4 frame
(f) Slot the solenoids into the holders (friction fit) and screw the holders into the back of the 3D printed structure
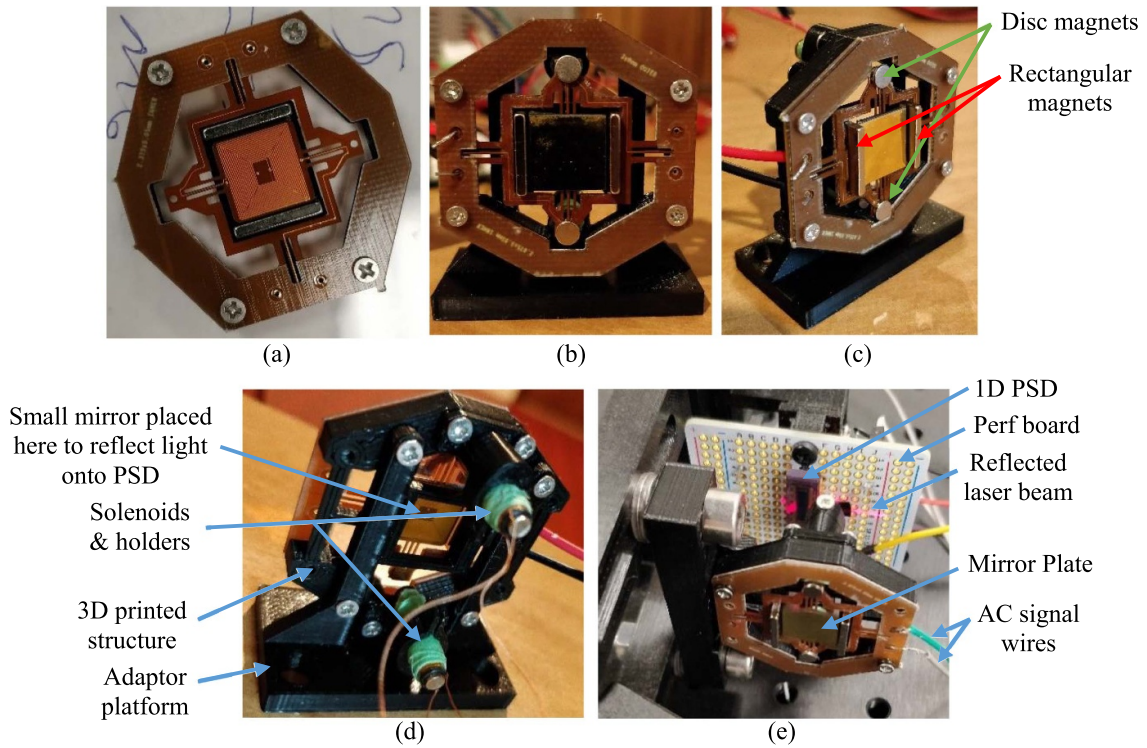
Figure 13. Assembled 2D FPCB micromirror. (a) FPCB structure. (b) Front view. (c) Isometric view. (d) Mirror backside. (e) 2D FPCB micromirror with 1D PSD for sensing angles.
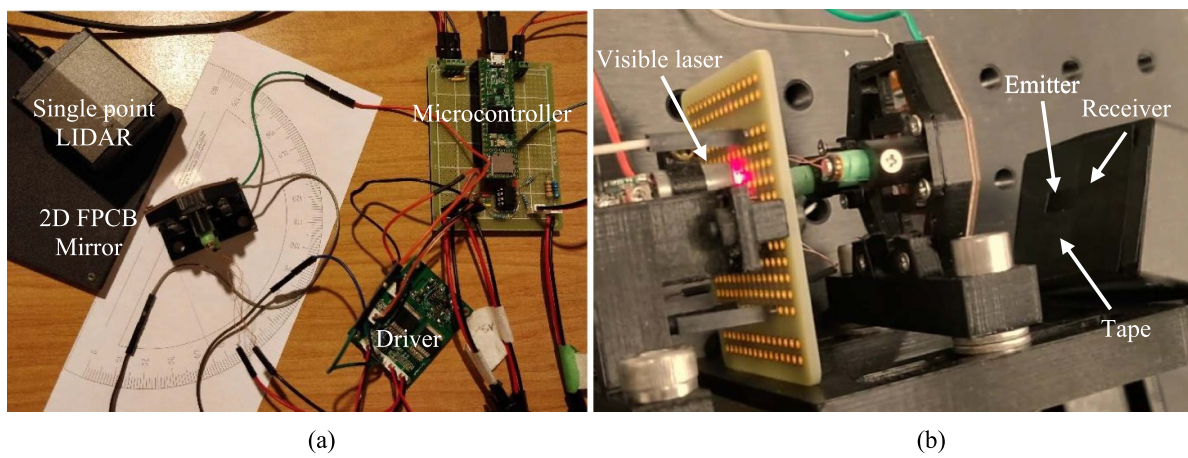

Figure 14. 3D LIDAR system. (a) Early prototype setup. (b) 3D LIDAR system with PSD.

(g) Screw in the 3D printed structure into an adaptor platform to be surface mounted for alignment

(h) Align a visible laser to the mirror behind the FPCB substrate/platform

(i) Place a PSD in the line of the reflected laser light from the visible laser

(j) Place a single point LIDAR in front of the 2D FPCB micromirror

The electronics in the system can be seen in figure 14(a). A Teensy 3.5 microcontroller is used to collect range data by the Benewake TF03 single point LIDAR [39] and send the data to the computer, and a driver is used to increase signal power from function generators to drive the 2D FPCB micromirror. The circuit of the driver can be found in appendix A. Figure 14(b) shows the pin holed visible laser which is used to thin the beam width since the mirror behind the FPCB is quite small (Ø3 mm), as well as the emitter and receiver positions on the single point LIDAR. The aperture of the sensors of the single point LIDAR can be seen being suppressed with tape. Part of the emitter and receiver are blocked in order to ensure all emitting laser light is reflected by the 2D FPCB micromirror aperture as well as much as possible scattered reflected light is reflected back to the receiver. According to the single point LIDAR manufacturer, the blocking tape can be eliminated if a customized single point LIDAR is ordered by
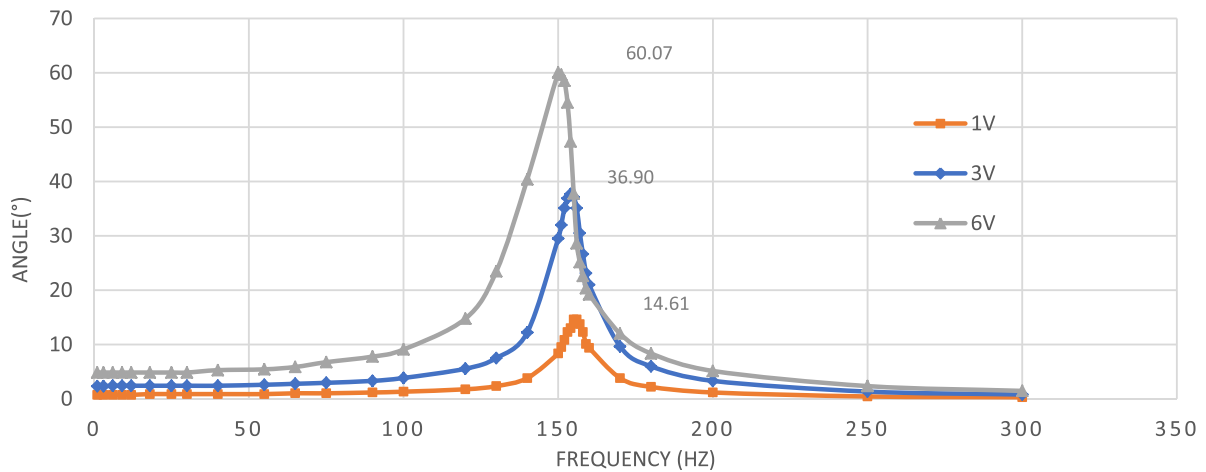
Figure 15. Optical angle of the oscillation about the inner axis vs frequency at various voltages.

reducing the distance between the emitter and receiver, as well as slightly reducing the emitter/receiver's apertures without affecting the performance.

5.2. 2D FPCB micromirror oscillation about inner axis testing

The rotation angle of the 2D FPCB micromirror is measured at various frequencies ranging from 0 to 300 Hz at several driving voltages. Figure 15 shows the resonant frequency of oscillation about the inner axis changes depending on the applied voltage. For example, at 6 V the max field of view (FOV) at resonant frequency is 60°, but at 3 V the max FOV is 36.9° at a higher frequency of 155 Hz.

The tested frequency peaks show that when the driving voltage (current) is higher, the frequency at the peak lowers as shown in figure 15. This could be attributed to the nonlinearity of the flexure material (polyimide), non-uniform magnetic field and non-linear torque versus the rotation angle.

The mode 2 and mode 3's frequencies are not very far away from each other. It is possible there would be cross-talk between the two modes. However, the experimental testing used the scanning angle to judge the rotation vibration magnitude, even if there is cross-talk (i.e. mode 2 and mode 3 are both activated), the rotation mode (mode 2) is obvious and the rotation (not the translation from mode 3) can be used for scanning the laser beam, such as to form the scanning LIDAR. In the future design, a bigger difference in mode 2 and mode 3 frequencies should be considered to avoid any cross-talk between the rotation and translation modes.

5.3. Testing of the 2D FPCB micromirror oscillation about outer axis testing

Static oscillation about the outer axis is conducted and the result is shown in figure 7(b). The tested rotation optical angle about the outer axis increases with the applied voltage. However, the rotation angle shows a plateau when the voltage and the rotation angle are high (e.g. >7 V and optical angle >8°). This is because the increasing of the electromagnetic field strength with the current applied to the solenoid coils starts to
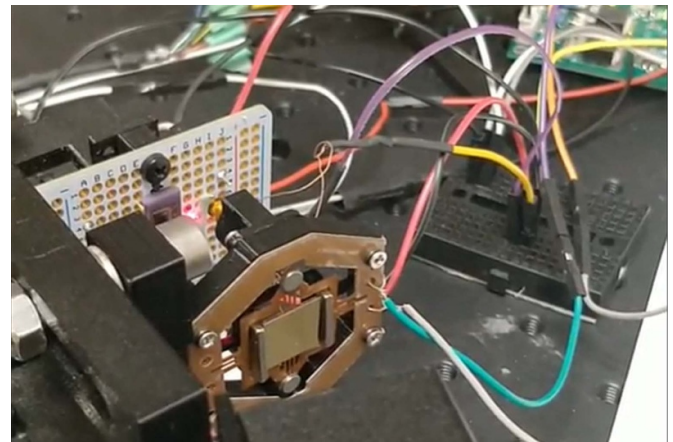

Figure 16. Testing the 2D FPCB micromirror with PSD tracking angles.

be not as sharp as that at low current when the current/voltage is high. In addition, the magnetic discs become unparalleled to the solenoid core when the rotation angle become large, that decreases the force component in the direction perpendicular to the discs' surface which contribute to the rotation of the gimbal. Figure 16 shows the testing setup for the 2D FPCB micromirror.

5.4. Testing of the 3D LIDAR based on the 2D FPCB micromirror

The testing result of the 3D LIDAR based on the 2D FPCB micromirror is shown in figure 17. A few videos in [40] show the operation of the 2D FPCB micromirror as well as demonstrations of the 3D LIDAR based on the 2D micromirror. The colors in figure 17 are mapped based on the distance values of a point in the point-cloud in *x, y, z* directions. All colors are distances mapped to 8-bit color (0–255). Increasing values of red are mapped along the *x*-direction (red ticked line), increasing values of green are mapped along the *y*-direction (green ticked line), and increasing values of blue are mapped along
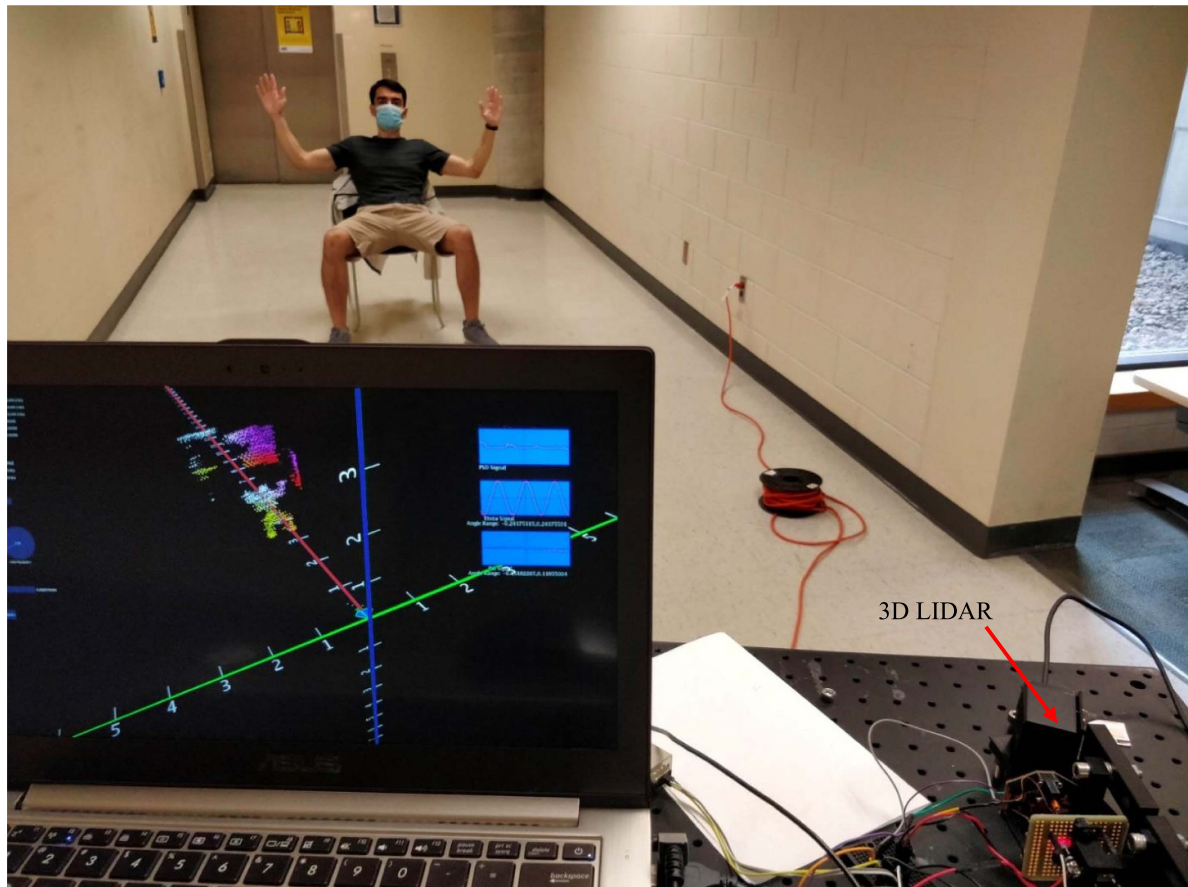
Figure 17. Testing 3D LIDAR based on the 2D FPCB micromirror.

the *z*-direction (blue ticked line). The algorithm for this mapping is described in appendix B. The mapping for the *x*-axis (depth) was preset to 5 for the upper bound, which unfortunately removes red from any points deeper than 5 m.

Since the 3D LIDAR reported in this paper can only cover 40° horizontally, nine such LIDARs are needed in order to cover 360°. For example, multiple such LIDARs can be mounted along the circumferential of the vehicle for full 360° coverage.

6. Conclusion and discussion

This paper developed a 2D FPCB micromirror and a 3D LIDAR based on the 2D micromirror. The 2D FPCB micromirror retains the benefits of previously developed 1D FPCB micromirror, i.e. large mirror aperture and low cost. Prototypes of the 2D FPCB micromirror and the 3D LIDAR based on it are fabricated and tested. The test results demonstrate that the 2D FPCB micromirror based 3D LIDAR achieved a volume reduction over the previous 1D FPCB micromirror based 3D LIDAR from 1042 cm^3 to 754 cm^3, a mass reduction from 250 g to 150 g

The scanning angles of both the oscillation about the inner axis and outer axis can be further improved using vacuum packaging of the micromirror as reported in [41]. The current in the solenoids can also be increased within the maximum

allowed current limit to increase the torque generated by the solenoids such as to increase the frequency oscillation about the outer axis since stronger torsion beams can be used. When converting the distance to colors to plot the image map, the software uses limited color levels instead of continuum of colors, and the scaling of the distance conversion to color is not able to clearly show all distance differences very obviously, or the color resolution is not adequate. This should be improved in the future.

The design of using solenoids for outer axis oscillation does not necessarily lead to low frequency due to the extra moment of inertia brought by the permanent magnet. This is because the design of using solenoids for the outer axis oscillation is normally for a large aperture mirror, of which the overall moment of inertia is quite high due to the large size of the mirror plate. The extra moment of inertia brought by the permanent magnetic discs is not very significant. For example, in the design reported in this paper, the moment of inertia brought by the two permanent discs are only about 3% of the overall moment of inertia of the oscillation parts about the outer axis.

Data availability statement

All data that support the findings of this study are included within the article (and any supplementary files).

Appendix A. Driver circuit schematic
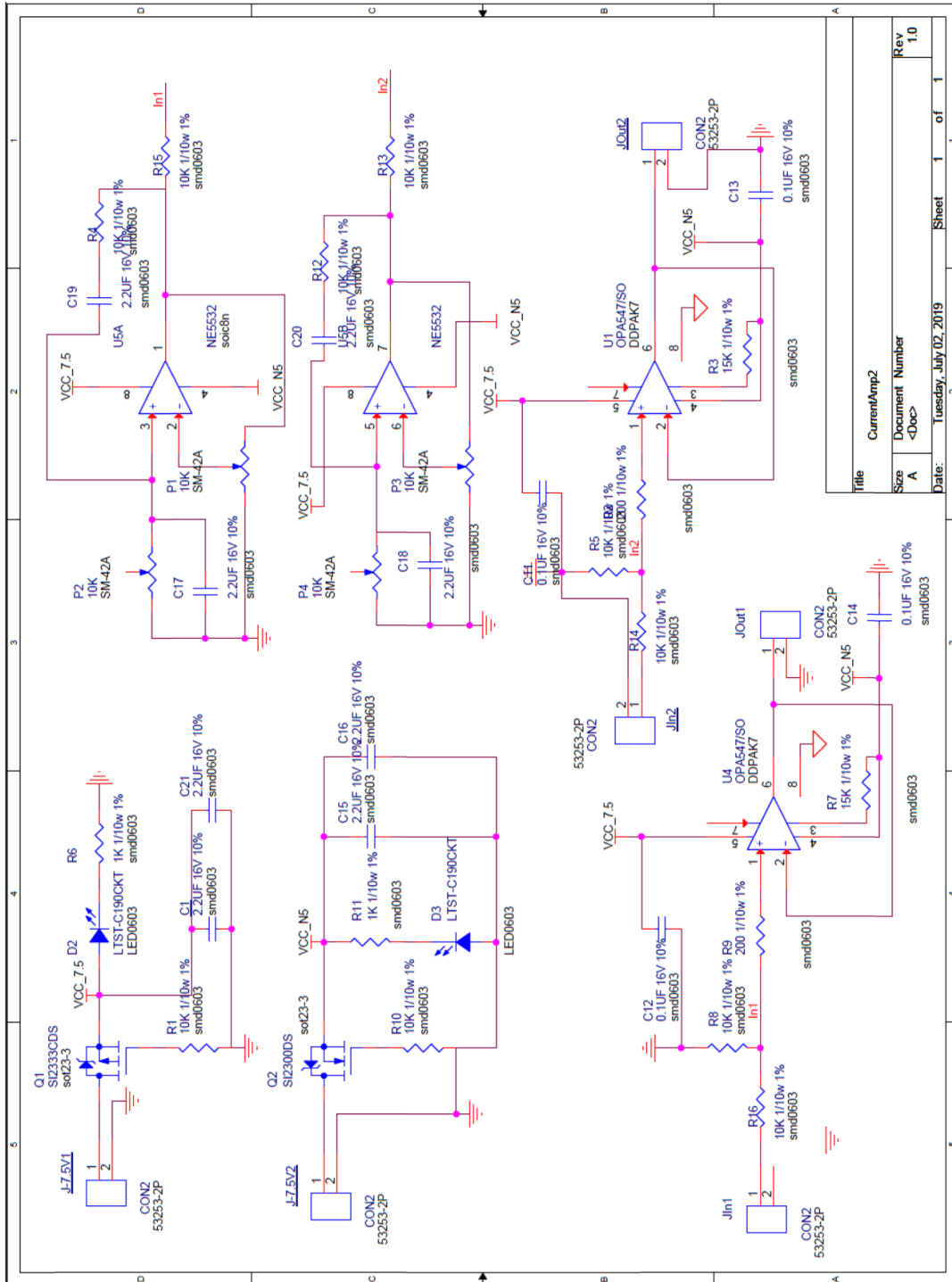
Appendix B. Color mapping algorithm

The algorithm used for the colors are as follows:

R = map(*x, x*B, 5, 0, 255)
G = map(*y, y*B, 8, 0, 255)
B = map(*z, z*B, 30, 0, 255)
stroke(R,G,B)
point(*x,y,z*)

Note that the map() function works by taking the 1st parameter and maps it from the range between the 2nd and 3rd parameters to a range within the 4th and 5th parameters. The stroke() function modifies the color of the point by RGB values between 0–255, hence the 0–255 bound on the map function. The point() function plots the *x, y, z* coordinates in 3D space with the stroke() function's RGB values. *x, y, z* are the point coordinates in 3D space, while *x*B, *y*B, *z*B are variables for the lower bound of the mapping. The upper bound is pre-set to 5, 8, 30 for R, G, B.

ORCID iDs

Trevor S Tai ⓘ https://orcid.org/0000-0001-5569-3690
Siyuan He ⓘ https://orcid.org/0000-0002-6954-1206
Behrad Ghazinouri ⓘ https://orcid.org/0000-0002-1257-6870

References

[1] Atanacio-jiménez G, Hurtado-ramos J B and González-barbosa R 2011 LIDAR velodyne HDL-64E calibration using pattern planes *Int. J. Adv. Robot. Syst.* **8** 70–82
[2] Yoo H W, Druml N, Brunner D, Schwarzl C, Thurner T, Hennecke M and Schitter G 2018 MEMS-based lidar for autonomous driving *Elektrotech. Inf.tech.* **135** 408–15
[3] Kimoto K, Asada N, Mori T, Hara Y, Ohya A and Yuta S 2014 Development of small size 3D LIDAR *Proc.—IEEE Int. Conf. on Robotics and Automation* pp 4620–6
[4] Ye L, Zhang G and You Z 2017 Large-aperture kHz operating frequency ti-alloy based optical micro scanning mirror for lidar application *Micromachines* **8** 120
[5] Weibring P, Edner H and Svanberg S 2003 Versatile mobile lidar system for environmental monitoring *Appl. Opt.* **42** 3583–94
[6] Noda S *et al* 2018 Development of coaxial 3D-LiDAR systems using MEMS scanners for automotive applications *Proc. SPIE* **10757** 107570E
[7] Kasturi A, Milanovic V, Atwood B H and Yang J 2016 UAV-borne lidar with MEMS mirror-based scanning capability *Proc. SPIE* **9832** 98320M
[8] Holmström S T S, Baran U and Urey H 2014 MEMS laser scanners: a review *IEEE J. Microelectromech. Syst.* **23** 259–75
[9] Van Kessel P F, Hornbeck L J, Meier R E and Douglass M R 1998 A MEMS-based projection display *Proc. IEEE* **86** 1687–704
[10] Aksyuk V A *et al* 2003 Beam-steering micromirrors for large optical cross-connects *J. Lightwave Technol.* **21** 634–42
[11] Milanović V, Matus G A and McCormick D T 2004 Gimbal-less monolithic silicon actuators for tip-tilt-piston micromirror applications *IEEE J. Sel. Top. Quantum Electron.* **10** 462–71
[12] Pan Y, Xie H and Fedder G K 2001 Endoscopic optical coherence tomography based on a microelectromechanical mirror *Opt. Lett.* **26** 1966
[13] Jain A, Kopa A, Pan Y, Fedder G K and Xie H 2004 A two-axis electrothermal micromirror for endoscopic optical coherence tomography *IEEE J. Sel. Top. Quantum Electron.* **10** 636–42
[14] He S and Ben Mrad R 2003 Development of a novel translation micromirror for adaptive optics *Proc. SPIE* **5264** 154–61
[15] He S and Chang J S 2009 Experimental verification of an out-of-plane repulsive-force electrostatic actuator using a macroscopic mechanism *Microsyst. Technol.* **15** 453–61
[16] He S and Ben Mrad R 2005 Large-stroke microelectrostatic actuators for vertical translation of micromirrors used in adaptive optics *IEEE Trans. Ind. Electron.* **52** 974–83
[17] He S and Ben Mrad R 2006 Performance assessment of a multi-level repulsive-force out-of-plane microelectrostatic actuator *Can. J. Electr. Comput. Eng* **31** 71–75
[18] He S and Ben Mrad R 2008 Design, modeling, and demonstration of a MEMS repulsive-force out-of-plane electrostatic micro actuator *J. Microelectromech. Syst.* **17** 532–47
[19] Wang D, Watkins C and Xie H 2020 MEMS mirrors for LiDAR: a review *Micromachines* **11** 456
[20] Zuo H and He S 2016 FPCB micromirror-based laser projection availability indicator *IEEE Trans. Ind. Electron.* **63** 3009–18
[21] Zuo H and He S 2017 Double stage FPCB scanning micromirror for laser pattern generation *Proc. IEEE Int. Conf. on Industrial Technology* (*Toronto, Canada, 23–25 March*) pp 917–21
[22] Zuo H and He S 2017 FPCB ring-square electrode sandwiched micromirror-based laser pattern pointer *IEEE Trans. Ind. Electron.* **64** 6319–29
[23] Zuo H and He S 2018 Double stage FPCB scanning micromirror for laser line generator *Mechatronics* **51** 75–84
[24] Periyasamy K G K, Zuo H and He S 2019 Flexible printed circuit board magnetic micromirror for laser marking/engraving *J. Micromech. Microeng.* **29** 085001
[25] Zuo H and He S 2019 1D LiDAR based on large aperture FPCB mirror *Int. Conf. on Optical MEMS and Nanophotonics*, (*28 July–1 August 2019*) (Daejeon: KAIST) pp 150–1
[26] Tan J V and He S 2019 Electromagnetic FPCB micromirror scanning laser rangefinder *Int. Conf. on Optical MEMS and Nanophotonics* (*July 2019*) pp 186–7
[27] Periyasamy K G K, Tan V J, He S and Kourtzanidis N 2019 External electromagnet FPCB micro-mirror for large angle laser scanning *Micromachines* **10** 1–9
[28] Tan V J and He S 2020 Oscillation FPCB micromirror based triangulation laser rangefinder *J. Micromech. Microeng.* **30** 95008–22
[29] Zuo H and He S 2021 Extra large aperture FPCB mirror based scanning LiDAR *IEEE/ASME Trans. Mechatronics* **27** 93–102
[30] Tai T S and He S 2022 3D LIDAR based on FPCB mirror *Mechatronics* **82** 102720
[31] Zuo H and He S 2020 FPCB masked one-step etching large aperture mirror for LiDAR *IEEE J. Microelectromech. Syst.* **29** 571–84
[32] Ghazinouri B, He S and Tai T S 2022 A position sensing method for 2D scanning mirrors *J. Micromech. Microeng.* **32** 045007
[33] Magnetics K J 2019 Demagnetization (BH) curves for neodymium magnets (available at: www.kjmagnetics.com/bhcurves.asp)

[34] KAPTON®HN 2008 *Polyimide Film Technical Data Sheet* (Circleville, OH: DuPont) (available at: https://docs.rs-online.com/c6e2/0900766b80659d8c.pdf)

[35] He W, Goudeau P, le Bourhis E, Renault P-O, Dupré J C, Doumalin P and Wang S 2016 Study on Young's modulus of thin films on Kapton by microtensile testing combined with dual DIC system *Surf. Coat. Technol.* **308** 273–9

[36] ANSYS 2020 *Release 2020 R1 Documentation for ANSYS®* (Canonsburg, PA: ANSYS Inc)

[37] Grant I S and Phillips W R 1990 Manchester Physics *Electromagnetism* 2nd edn (New York: Wiley)

[38] On-Trak 2019 *1L Series—single-axis Position Sensing Detectors* (Irvine, CA: On-Trak Photonics Inc) (available at: www.on-trak.com/1lseries.html)

[39] Benewake 2019 TF03 IP67 LiDAR distance sensor (Benewake (Beijing) Co.) (available at: http://en.benewake.com/product/detail/5c345cc2e5b3a844c472329a#case)

[40] Tai T S, He S and Ghazinouri B 2022 2D micromirror demo videos (available at: https://drive.google.com/drive/folders/1RrXkHoJAEfwPRYodYTafIaCO4CBfCFEt?usp=sharing)

[41] Hofmann U, Janes J and Quenzer H-J 2012 High-Q MEMS resonators for laser beam scanning displays *Micromachines* **3** 509–28